Experimental Thermal and Fluid Science 119 (2020) 110198

Contents lists available at ScienceDirect

Experimental Thermal and Fluid Science

journal homepage: www.elsevier.com/locate/etfs

Using fiber-optic sensors to give insight into liquid-solid phase transitions in pure fluids and mixtures

Markus Solberg Wahl[a,*,1], Øivind Wilhelmsen[b,c], Dag Roar Hjelme[a]

[a] Norwegian University of Science and Technology (NTNU), Department of Electronic Systems, 7491 Trondheim, Norway
[b] Norwegian University of Science and Technology (NTNU), Department of Energy and Process Engineering, 7491 Trondheim, Norway
[c] SINTEF Energy Research, 7034 Trondheim, Norway

ARTICLE INFO

Keywords:
Phase transitions
Fiber optic sensors
Multimode interference
Fiber Bragg grating

ABSTRACT

Fiber optic sensors offer a new and unique way to detect and analyze phase transitions, due to their small thermal mass and inert material. This paper presents and demonstrates a dual-sensor system to detect and analyze phase transitions in pure water and aqueous ethanol mixtures. With a multi-mode interferometer based on a thin-core fiber, and a fiber Bragg grating sensor, it is possible to differentiate between refractive index, temperature and strain in the sample system. The three parameters supply important information during a phase transition, but also in the characterization of the liquid and solid phases. Binary mixtures at non-eutectic concentrations are expected to separate into a solid phase consisting of only one constituent, and the sensors are demonstrated to be able to estimate the concentration in the remaining liquid phase. For pure water and low ethanol concentrations, the progression of the phase transition was found to be limited by heat transfer, whereas for higher concentrations the process becomes mass transfer limited. In pure water, strain due to thermal expansion of the ice hinderes temperature measurements in the solid phase. The reflection-based geometry enables insertion probes that measure the properties inside the samples, with little or no disturbance of the system. By interpreting the sensor response in a known system, the sensing capabilities in unknown substances can be evaluated. The sensor system is able to capture the dynamics of the phase transition, which can be difficult to predict theoretically due to the multitude of contributing effects. Analysis of the combined signal from the two sensors enables the determination of the ethanol mixture melting points in agreement with the literature, within the uncertainty of the system (0.25 K).

1. Introduction

A fundamental understanding of phase transitions is important both in industrial processes and for research purposes. To detect the onset of a phase transition, and to monitor its subsequent progression, is paramount in fields such as in energy storage systems based on latent heat [1], food technology [2], the pharmaceutical industry [3], and liquefaction of hydrogen [4,5]. Understanding and control of the liquid-to-solid transition is also important in biology and in fixation of biological tissue for optical microscopy [6,7].

Because the nucleation and growth that initiates a phase transition is stochastic in nature, accurate detection is important [8]. Detecting the phase transition directly can aid in confirming, creating, or alleviate the need for a prediction. Because ethanol is miscible in both polar and non-polar substances, it is a versatile solvent in a wide range of industries (e.g., chemical, pharmaceutical, food and fuel)[9]. Studies have shown that refractometric analysis of aqueous ethanol mixtures is challenging due to anomalies in the physical–chemical properties, such as hydrophobic solute association and the formation of ethanol clusters [10,11]. Freezing of such binary mixtures, has been widely studied [12–15] and it is accepted that the solid phase that forms is pure ice i.e. it consists of only water molecules. This entails that the concentration in the remaining liquid phase, and its associated properties, change during the phase transition.

Classical techniques to detect liquid-to-solid transitions include differential scanning calorimetry [12,15] and differential thermal analysis [6,16], which measure the difference in heat exchange and temperature, respectively, as the temperature is scanned over the interval where a phase transition is expected to occur. Although these techniques give important information on phase transitions, the

* Corresponding author.
E-mail address: markus.s.wahl@ntnu.no (M.S. Wahl).
[1] This document is the result of the research project funded by InterReg Sweden-Norway program [IR2015.01] and the ENERSENSE research initiative.

https://doi.org/10.1016/j.expthermflusci.2020.110198
Received 31 October 2019; Received in revised form 3 June 2020; Accepted 4 June 2020
Available online 10 June 2020

experimental setup is complicated and not well suited for industrial application, and it does not allow for measurements in specific points in the sample or a reactor. It is also possible to detect liquid–solid transitions by measuring the changes in conductivity. A current is sent through the sample and an increase in impedance indicates solidification [2]. Because phase transitions are either exothermic or endothermic, they can also be detected by measuring the temperature changes locally, using electronic temperature sensors (e.g., thermocouples). However, these sensors may disturb the measurements by acting as heat sinks/sources, and thus affect the temporal response due to their thermal mass [17]. For transparent materials, phase transitions can also be observed visually, if they cause a change in the transparency. However, this requires transparent containers or windows [18], which may not always be feasible in the design of the measurement rig or reactor.

General advantages of fiber optic sensors in experimental thermophysics and thermochemistry include the inert glass material of optical fibers, their robustness and small size. This enables sensors with a small thermal mass, which minimize the influence on thermodynamic processes. This is ideal for accurate measurements in small sample sizes, or where heat flow is a limiting factor. Optical fibers made of fused silica also remain flexible at cryogenic temperatures [19], which makes them robust and especially well suited in low temperature sensing. Immunity to electromagnetic interference, high sensitivity, low cost and the possibility for remote sensing are other advantages that motivate the use of fiber optic sensors.

Researchers have in recent years developed fiber optic sensors to detect and study phase transitions [20–24]. Han et al. detected the phase transition in n-octadecane by utilizing the different refractive index (RI) in the solid and liquid states. For N-octadecane, these values happen to be above and below the RI of the fiber, which enables the distinction of phases based on a guiding- or no-guiding-condition. This was demonstrated both in a multi-mode fiber interferometer [20] and a Fresnel reflection probe [24]. Also based on changes in reflectivity, Mani et al. [23] detected freezing of aqueous NaCl-solutions. These Fresnel-reflection sensors offer a mechanically robust point measurement of the aggregate state, as only the cleaved end-face of a single-mode fiber (SMF) is required to be in contact with the sample. However, the small interface with the sample makes the technique sensitive to irregularities such as bubbles or impurities that may be present in the sample. A method with a larger sample interface to average over was presented by Millo et al. [21], who performed evanescent field attenuation spectroscopy in the infrared (IR) range to detect the freezing event in water and heavy water. However, the transmission configuration and the need for specialty fibers that are transmissive in the IR complicates the experimental implementation. Kumar et al. [22] used a fiber-optic multi-mode interferometer to measure micro-strain induced by the solidification of paraffin wax.

This paper presents a novel dual-sensor setup to detect and study phase transitions, based on well-known fiber-optic sensor technologies. It consists of a fiber-optic multi-mode interferometer [25], interrogated in reflection, together with a fiber Bragg grating (FBG) sensor [26]. The sensors and the interrogation setup are depicted in Fig. 1. The RI sensitivity of the multi-mode interferometer enables detection of all phase transitions that cause a change in RI. However, the interferometer is also sensitive to temperature and strain [27,28]. To distinguish between these parameters, an FBG sensor is used, which is also sensitive to temperature and strain, but not to RI. Under the assumption that a liquid material imparts an insignificant strain on the sensors, any deviations from the FBG sensor temperature sensitivity in the solid phase can be attributed to strain. The dual-sensor setup can therefore be used to distinguish between these parameters, which implicitly also lead to measurement of parameters such as sample concentration, freezing point, melting point and latent heat.

The reflection-based geometry of the fiber-optic sensors creates insertion probes that are clamped only in one end. This simplifies the implementation, and alleviates thermally induced bending stress that may occur in transmission-based sensors. This sensor can therefore give information on both the liquid and solid phase, in addition to the transition itself.

The next section will present the dual-sensor configuration and the measuring procedure. The results for measurements in pure water and the binary mixtures of ethanol and water will then be presented and discussed to highlight the amount of information obtained from the sensor setup. By interpreting the results in a known system, it is showed how the sensor response can be utilized to examine substances with unknown properties. Throughout the paper, a distinction between the freezing point and the melting point of the sample will be upheld.

2. Experimental methods

The experimental setup is illustrated in Fig. 1, showing the sensor configuration (left) and the measurement rig (right). The optical interrogation setup consists of a broadband source (FYLA, SCT500), a grating-based spectrometer with 0.3 nm resolution (Ibsen I-MON 512), and a 2 × 2 coupler (Thorlabs, TW1550R5A2). The sensors are connected to the remaining two arms of the coupler. The FBG sensor (Optromix) is inscribed in an SM1500 fiber with a reflectivity of 79% and full-width half-maximum (FWHM) of 0.2 nm. The multi-mode interferometer is fabricated by splicing a 14.2 mm section of thin-core (TC) fiber (SM400) to the end of a single-mode fiber (SMF). The core-diameter mismatch causes cladding modes to be excited in the TC fiber, which create the interference spectrum. To ensure good visibility in the interference spectrum, the cleave angles were confirmed to be smaller than 0.1 degrees [25]. To increase the reflected signal, a silver mirror was deposited at the end-face of the fiber by the mirror reaction [29]. The fiber was placed in contact with the reactant solution and withdrawn carefully without breaking the meniscus created by surface tension. By monitoring the reflected signal during silver deposition, the process could be ended when the reflectivity reached its maximum (~66%). Inspection with an optical microscope showed an approximate mirror thickness of 60 μm. To achieve comparable signal intensities from the two sensors, a variable fiber-optic attenuator was placed between the coupler and the FBG sensor. A band-pass filter was also used to block wavelengths outside the range of the spectrometer (1510–1610 nm).

The FBG sensor has a strong reflection peak at a wavelength, λ_B given by [26]:

$$\lambda_B = 2n_{eff}\Lambda, \tag{1}$$

where n_{eff} is the effective RI of the grating and Λ is the grating period. A change in the temperature, ΔT will affect both the effective RI and the period of the grating due to the thermo-optic effect and thermal expansion. The change in wavelength can be expressed as [30]:

$$\Delta\lambda_B = \lambda_B(\alpha + \xi)\Delta T \tag{2}$$

where α is the thermal expansion coefficient, and ξ is the thermo-optic coefficient, which accounts for approximately 95% of the temperature sensitivity [26]. The sensitivity to strain was found to be approximately 1 pm/$\mu\varepsilon$ in previous work [26].

The interference spectrum from the TC sensor exhibits intensity dips at wavelengths where the modes interfere destructively. The wavelength of the i'th dip, $\lambda_{dip,i}$ can be expressed as:

$$\lambda_{dip,i} = \frac{4L[n_{eff}(\lambda, n_{ext}) - n'_{eff}(\lambda, n_{ext})]}{2i - 1}, \tag{3}$$

where L is the length of the interferometer, n_{eff} and n'_{eff} is the effective index of two modes at wavelength λ and external (sample) RI (n_{ext}). Because of the evanescent field extending beyond the boundaries of the fiber, the effective indices of the modes depend on the external RI. The interference spectrum will therefore shift based on the RI surrounding the sensor. As explained in [25], this sensitivity to the external RI can

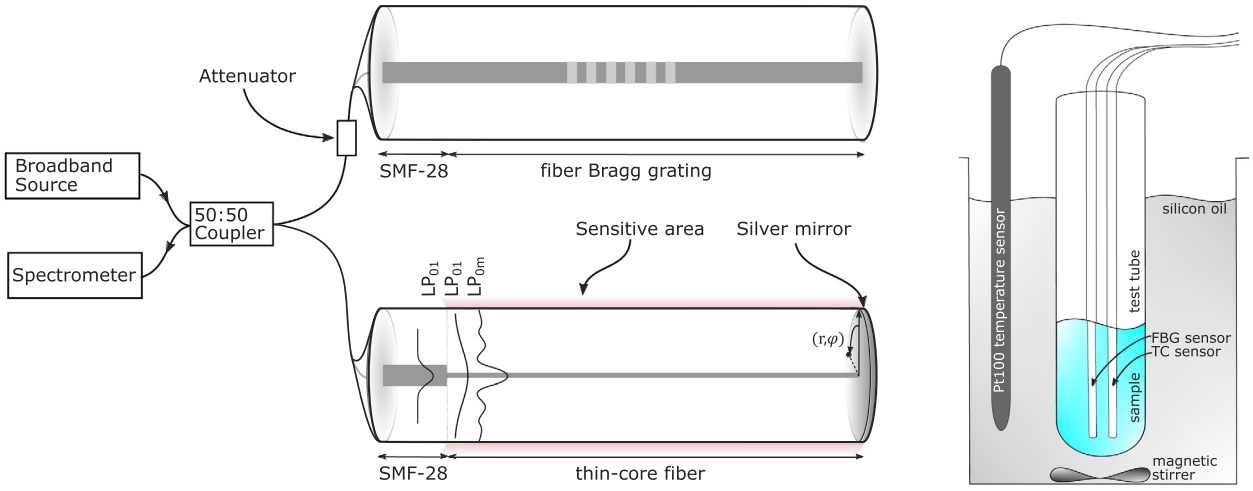

Fig. 1. Schematic of the experimental setup. The fiber-optic sensor system (left) consists of a broadband source, a spectrometer, a 50:50 fiber optic coupler and the two sensors (fiber Bragg grating (FBG) and thin-core (TC) interferometer). Both sensors reflect light at wavelengths dependent on their temperature and strain, whereas only the TC-sensor is sensitive to the RI of the surroundings. The fiber-optic attenuator is used to get comparable signal intensities from the two sensors. The measurement rig (right) consists of a temperature bath filled with silicon oil, an electrical Pt100 temperature sensor and a test tube holding the sample liquid. The two sensors are placed inside the sample.

be expressed as

$$\frac{d\lambda_{dip}}{dn_{ext}} = \frac{\lambda_{dip}}{(n_g - n_g')}\left(\frac{\partial n}{\partial n_{ext}} - \frac{\partial n'}{\partial n_{ext}}\right) \tag{4}$$

where n_g and n_g' is the group velocity of the same two modes. This shows that it is the difference in sensitivity to the external RI of the two modes that cause the RI sensitivity of the interferometer.

The temperature sensitivity appears because both n_{eff} and n_{ext} are functions of temperature. Although the thermo-optic coefficient of water is two orders of magnitude higher than that of the fiber material [31,32], the fiber properties dominate because of the high confinement factor. In this sensor, only 10^{-2}% of the electromagnetic field extends beyond the fiber boundaries, but this can be increased by etching the fiber with hydrofluoric acid [11].

A temperature bath (Hart Scientific, 7103 Micro-bath) with an accuracy of 0.25 K, was used to perform the temperature scans (Fig. 1, right). An additional temperature sensor (3-wire, Pt100) with a stainless steel sheath, was placed in the silicon oil bath fluid. The fiber-optic sensors were secured 1 mm apart inside a test tube (Borosil, 27 ml), with the sample placed 10 cm below the silicon oil surface. The temperature bath has a stated temperature uniformity of ±0.2 K, which should ensure uniform conditions in the sample. The test tube was left open at the top to keep the sample at atmospheric pressure. A LabVIEW program was developed to control the temperature setpoints and scan rate in the temperature bath, and for acquiring data from the Pt100-sensor and the spectrometer. The output was logged every 20 s. Additionally, a digital boroscope was placed in the temperature bath to visually monitor the process, and capture images and videos.

The samples were prepared with deionized water (< 1.5μS/cm) mixed with 96% Ethanol (VWR) by weight. From the uncertainty disclosed by the manufacturer, the estimated error in the concentration of the prepared mixtures was 0.4%. The mixtures were heated to 50°C for 5 h and subsequently stored for one week to let the mixtures equilibrate, in accordance with the recommendations by Takaizumi et al. [13]. 6 mL of sample fluid was placed in the test tube before the fibers were inserted. The fiber-optic sensors were clamped in a way that ensured that they had the same position in the test tube each run. The samples were then let to stabilize at 30°C for 15 min, which was necessary to achieve reproducible results, especially at higher ethanol concentrations. The temperature scans were performed with a cooling rate of 0.2°C/min down to −30°C, and heating rate of 0.1°C/min back to 30°C. Prior to all measurements, the test tube and the optical fibers were rinsed with acetone, 96% ethanol and DI water, to remove any contaminants.

Freezing of water into ice occurs when an ice nucleus appears that is larger than the critical size for further growth [8]. This is a statistical process that is driven by the degree of metastability i.e. a larger supercooling will increase the probability of a critical-size nucleus to initiate the phase transition. Because of the enthalpy of fusion, the freezing process will release latent energy that heats the sample. This limits the amount of solids that can be produced, as the sample cannot exceed its melting temperature [33]. Treating the system as adiabatic in the instant where the solid phase forms (freezing), the heat produced by the solidification (ΔQ_{ice}^{fus}) must be equal to the heat spent to heat up the sample. The energy balance then gives:

$$\Delta Q_{liq} + \Delta Q_{ice} = \Delta Q_{ice}^{fus}, \tag{5}$$

where ΔQ_{liq} and ΔQ_{ice} are the heat absorbed by the remaining liquid phase and the solid ice phase, respectively. This can further be formulated as:

$$C_p^{liq} m_{liq} \Delta T_s + C_p^{ice} m_{ice} \Delta T_s = \Delta H_{fus}^{ice} m_{ice}, \tag{6}$$

where C_p^{liq} and C_p^{ice} are the specific heat capacities of the liquid and ice, respectively, m_{ice} is the amount of ice produced, m_{liq} is the remaining liquid, ΔT_s is the supercooling, and ΔH_{fus}^{ice} is the enthalpy of fusion for ice. A greater supercooling or heat capacity of the liquid will therefore produce more solid when the sample freezes, and reduce the amount of additional heat that must be removed to freeze the remaining liquid. As the enthalpy of fusion decreases for higher ethanol concentration [15,34], more ice may initially be produced, and the subsequent crystal growth requires less heat to be transferred. We assume in the above equation that the heat capacities are approximately constant in the considered temperature interval.

3. Results and discussion

Snapshots of how the freezing of 10% ethanol progresses are shown in Fig. 2. In this case, the nucleation occurs in the bottom of the test tube and the crystal grows upwards. Where in the test tube and at what temperature the nucleation takes place, varies from experiment to

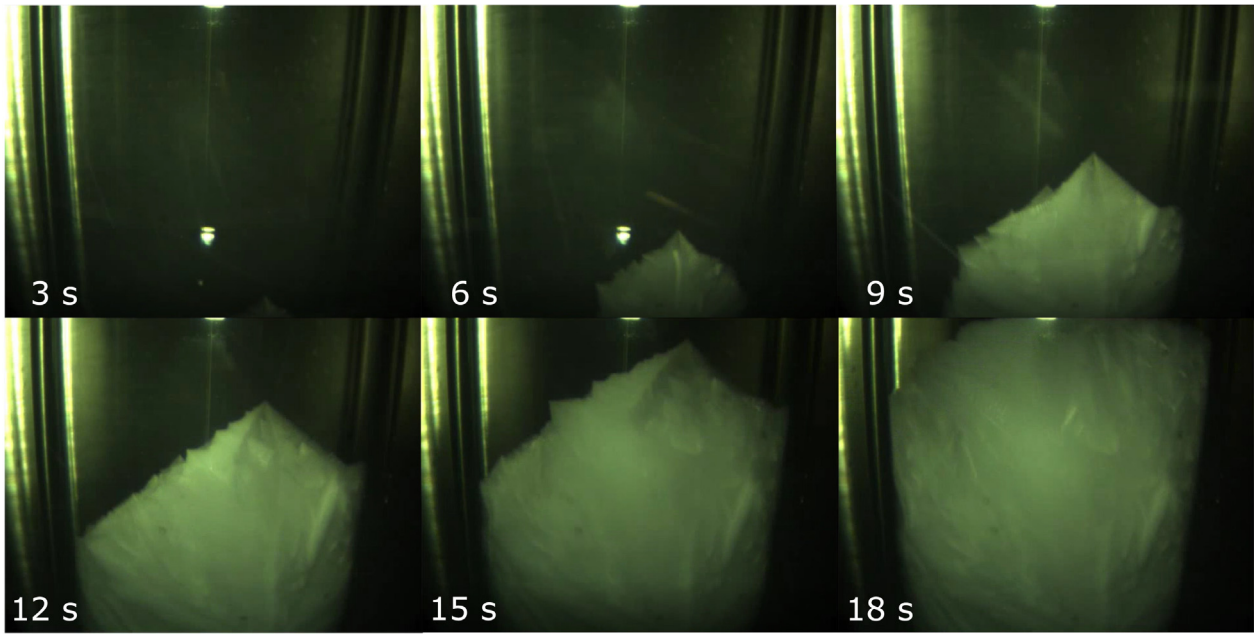

Fig. 2. Snapshots show the progression during freezing of 10% ethanol at 3 s time intervals. Multiple crystal facets are visible. The high crystallinity indicates high purity in the solid phase.

experiment. Higher concentrations were observed to slow down the crystallisation process, in agreement with [35,36].

An example of an output spectrum from the dual-sensor configuration is shown in Fig. 3. The three main interference dips and the FBG peak are highlighted. To accurately determine the wavelength of the dips, they were fitted to a fifth-degree polynomial over a 9 nm spectral range. The FBG peak wavelength was similarly found by curve-fitting a Gaussian function. In the following sections, the change in these wavelengths during the temperature scans will be presented and interpreted to analyze the phase transitions.

At constant temperature in the bath, the measured root-mean-squared error (RMSE) of the determined wavelengths were 1.4 pm and 5.7 pm for the FBG and TC sensor, respectively. With an FBG temperature sensitivity of 9.2 pm/°C, this gives a mean error of 0.15 °C. The TC sensor was measured to have an RI sensitivity of 51.6 nm/RIU at n = 1.3165 (pure water at 1550 nm). The FBG sensor is assumed to have a strain sensitivity of 1pm/$\mu\varepsilon$, based on previous results [26].

In the following, the results for the case of pure water will be presented and analyzed. First, the FBG response will be discussed, and the conclusions drawn here will then be used to analyze the response from the TC sensor. The treatment will then be expanded to include the binary mixtures of ethanol and water, where the FBG will be used as a temperature sensor inside the sample and the combined dual-sensor response will be discussed.

3.1. Freezing of pure water

To study the sensor response in pure water, the sensors were placed in a 6 mL sample and cooled down to −30°C, as described in the Sec. 2. Fig. 4 shows the wavelength of the FBG-peak during the experiment, both as a function of temperature (left) and time (right). Both plots show the same data, with the wavelength axis spanning both plots. The

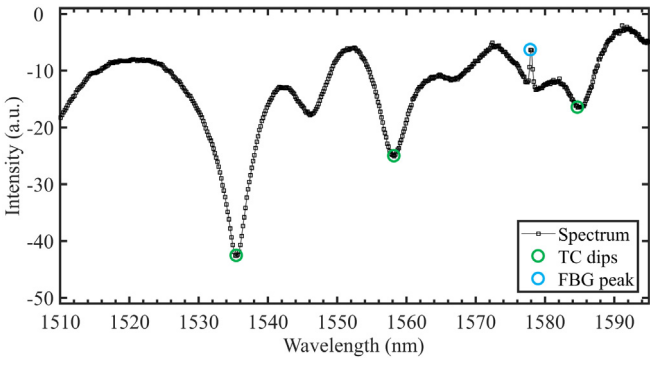

Fig. 3. A typical output spectrum, showing the sum of the reflected intensities from the two sensors as a function of wavelength. Three interference minima (dips) are identified, but only the first is used in interpreting the response. The peak from the FBG sensor has been attenuated as to not saturate the spectrometer, while ensuring acceptable visibility of the interference spectrum. The features of both sensors shift to longer wavelength (red-shift) with increasing temperature. The TC sensor red-shifts for increasing external RI. (For interpretation of the references to colour in this figure legend, the reader is referred to the web version of this article.)

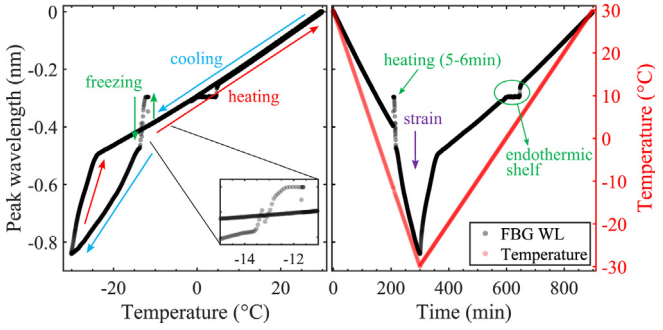

Fig. 4. The wavelength of the FBG-peak (Fig. 3) and how it shifts as a function of temperature and aggregate state of the surrounding medium. Both plots show the same data, as a function of temperature (left) and time (right). The measured temperature (Pt100) is plotted as a function of time (red). Upon cooling, the peak shifts to shorter wavelengths (blue-shift) until the freezing event causes a short-timed local heating (inset). The stronger blue-shift after freezing is due to strain. When the sample is reheated, the strain relaxes, and at 0°C, the ice starts to melt. The melting process keeps the local temperature constant until the whole sample has become liquid. (For interpretation of the references to colour in this figure legend, the reader is referred to the web version of this article.)

Table 1
Thermodynamic properties and calculated mass of ice created upon nucleation. The super-cooling (T_s) is the difference between the measured freezing temperatures and the melting points from the CRC Handbook [40]. The heat of fusion values were extracted from Kumano et al. [34] and the heat capacities from Rivkin et al. [41]. The amount of water originally present was calculated from the sample volume (6 mL) based on the densities of the mixtures.

Concentration:	0%	5%	10%	15%	20%	25%	30%
T_s (°C):	11.8°C	11.7°C	12°C	13.8°C	14°C	11°C	–
ΔH_{fus} (J/g):	333.55	328.9	320.6	308.8	293.2	274.1	251.3
C_p^{liq} (J/gK):	4.18	4.22	4.27	4.32	4.37	4.42	4.49
C_p^{ice} (J/gK):	2.108	2.108	2.108	2.108	2.108	2.108	2.108
Produced ice (g):	0.83	0.83	0.87	1.03	1.10	0.94	–
% of water:	13.8%	14.7%	16.4%	20.7%	23.5%	21.6%	–

measured temperature (Pt100) is also plotted as a function of time in the right plot (red). On cooling, the FBG-sensor is assumed to have no strain in the liquid, and the wavelength shifting to shorter wavelengths is therefore only due to the change in temperature (Eq. (2)). The shift in the liquid phase can therefore be used to create a baseline for the sensitivity, from which deviations must be caused by strain or a difference in temperature compared to what is measured outside the test tube in the bath fluid.

This difference can be observed when the water freezes at −11.8°C, which causes a sudden rise in temperature due to the release of latent heat. The peak shifts to a wavelength that corresponds to a temperature of 0°C. With a heat of fusion for ice of 333.55 J/g and an undercooling of 11.8°C, and assuming adiabatic conditions in the instant of freezing, calculations based on Eq. (6) estimate that only 0.83 g (14%) of ice is produced, see Table 1. Visual inspection showed that, contrary to the behavior seen in ethanol mixtures (Fig. 2), the initial solid phase in the pure water samples fills the whole sample volume with a slush or a dendritic ice structure in less than a second [37]. The small transient observed during the latter part of the freezing process is likely due to the random buildup of ice surrounding the fiber.

Further freezing requires additional heat transfer from the sample to the bath fluid. The heat transfer only facilitates the freezing of more water, and will not be able to cool the sample further until all liquid is frozen. According to the sensor output, this process takes around six minutes, after which the wavelength again continues to blue-shift. In the figure, this process is highlighted with green arrows and shown in higher detail in the inset, which shows the initial heating (red-shift) and the subsequent cooling and strain-induced blue-shift. The FBG sensor is hence able to detect the initial dendritic phase and the subsequent crystal growth [6].

3.1.1. The influence of heat flux on the detected strain

The initial blue-shift 60 pm below the baseline is attributed to the increased volume of ice over water, which causes strain on the sensor. Further cooling causes the FBG-peak to deviate further from the liquid baseline, which is interpreted as increased strain due to thermal expansion. This is consistent with increased compressive strain in the axial direction of the fiber due to ice compaction at lower temperatures [38], which is two orders of magnitude higher than that of the fiber [31]. By using the strain sensitivity from [26], the shift corresponds to a strain of approximately 300 $\mu\varepsilon$.

When the heating starts, the stress on the fiber seems to relax faster than it was built up during cooling, and the peak wavelength returns to the baseline already at −23°C. From the right plot, it can be seen that this process takes approximately one hour. During several repetitions of the experiment, most runs showed similar accelerated relaxation. It is an interesting effect as it initiates only when the sample is heated, and happens continuously over one hour. To investigate if the relaxation was due to the optical power causing local heating at the fiber tip, a measurement was conducted with the laser power reduced to 4%, which did not change the relaxation rate. Since the fiber extends out into room temperature, heat conduction through the fiber could also supply the heat necessary for the relaxation. Several heating and cooling cycles below 0°C were also performed to investigate whether the effect is caused by thermal expansion effects in the ice, or if the relaxation is due to slow slippage at the fiber-ice interface. This showed that upon every cooling stage, the increased stress on the fiber appeared, and was released at an increased rate during re-heating. For each cycle the strain decreased – during the fourth cool-down the strain response was halved. This may indicate some slippage of the fiber relative to the ice when the sample is heated. Only a decrease in thermal strain due to heat conduction through the fiber was found to support this behavior.

We emphasize that only sensor signals from the phases of the experiment deemed to be strain-free have been used to interpret results from the phase-transitions. Further discussions of strain therefore fall beyond the scope of the present work.

3.1.2. Melting of pure water

At the melting point (0°C), the peak wavelength remains constant until the bath fluid reaches 5°C. This shelf is interpreted as the sample having constant temperature, which is attributed to the endothermic melting of ice. To melt the 6 mL sample requires 2.1 kJ of heat, which is transferred slowly due to the low temperature difference. During this phase, the sample will remain at the melting temperature.

The temperature increase and retention during freezing and melting cannot be resolved by the temperature sensor (Pt100) outside the test tube. Having a temperature sensor with a small thermal mass therefore makes it possible to capture the dynamics of the phase transition.

3.1.3. Refractometric analysis of the phase transition

With the addition of an RI sensitive sensor, also the properties of the liquid and solid phases can be probed. Tracking the intensity dip created by the TC sensor in the same experiment as above gives the behaviour shown in Fig. 5. As this sensor is also sensitive to the RI surrounding the fiber, the temperature sensitivity becomes a convolution of the thermo-optic properties of both the fiber and the liquid. This is described by Eq. (3), where both n_{eff} and n_{ext} are functions of temperature. This enables further analysis of the properties of both the liquid and the solid phase.

As with the FBG-results (Fig. 4), the freezing event creates a red-shift to the wavelength that corresponds to a temperature of 0 °C. However, after the whole sample has become solid, the dip shows a large blue-shift of approximately 1.3 nm. This is comparable with the expected shift due to a difference in RI of 0.025 between water and ice

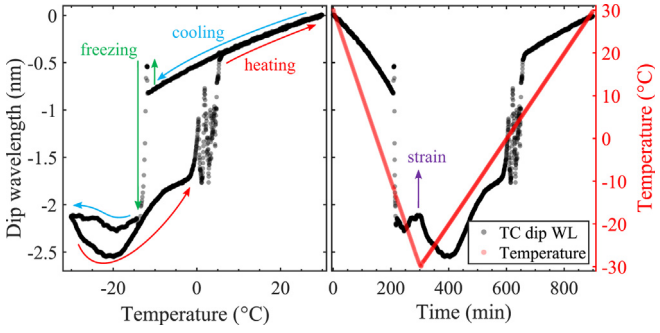

Fig. 5. The wavelength of the first TC interferometer dip (Fig. 3), from the same experiment as Fig. 4, as a function of temperature (left) and time (right). The same initial heating upon freezing is observed, but is in this case followed by a 1.2 nm blue-shift due to the lower RI of ice. Based on the results in Fig. 4, one can conclude that part of the shift in the solid ice i.s due to strain. (For interpretation of the references to colour in this figure legend, the reader is referred to the web version of this article.)

(51.6nm/RIU·0.025 = 1.29nm) [32]. The compressive strain seen earlier in Fig. 4 (200–400 min) can be seen to cause a red-shift in the TC sensor (right graph). The opposite direction of the strain-induced shift from the TC sensor is consistent with the results in [39] if compressive strain occurs in the axial direction. At 380 min, the FBG sensor indicates that the strain is released and the TC sensor pivots. The sensor may still be affected by some strain, but the sensitivity is now positive with regards to temperature (400–600 min). Although the thermo-optic coefficient of ice is negative, as it is for water above 4°C [32], the positive sensitivity is expected because the fiber temperature response dominates.

At 0°C, the intensity dip experiences large shifts during the melting, before it joins the liquid baseline. The total shift during the melting is approximately 1.3 nm, which corresponds to the total shift during the freezing. The large oscillations observed during the melting is attributed to the ice shifting during the melting process, exposing varying fractions of the fiber surface to liquid water. Movement of the remaining ice has been observed using the boroscope. The combined analysis of the two sensors emphasizes the benefits of having a dual-fiber setup, as discussed in the present work.

3.2. Freezing of ethanol mixtures

The FBG sensor result for the 10% sample is shown in Fig. 6. As in the results for pure water, the exothermic reaction heats the sample, which can be seen as a temporary red-shift in the cooling curve. However, due to the increased ethanol concentration in the remaining liquid phase, the melting point is continuously lowered as the freezing progresses. Contrary to the result for pure water, the temperature therefore decreases during the phase transition. When the freezing approaches completion, the cooling of the solid can proceed. The same effect can also be seen by comparing the endothermic shelves in Figs. 4 and 6. While the endothermic shelf in Fig. 4 is perfectly horizontal, the shelf in Fig. 6 exhibits a slope. This will be discussed further in Section 3.3.

As the sample regains equilibrium with the temperature bath, the response resumes its strain-free behavior. Because little or no strain is observed in the cooling process, the slightly shorter wavelength seen when reheating is probably not caused by strain, but rather by the continuous thawing of ice in binary mixtures over a finite temperature interval. This would keep the sample at a slightly lower temperature since additional heat must be supplied. However, the endothermic shelf observed in the pure water measurements reappears at −5°C until 2°C, where the remaining ice melts. The melting point of 10% ethanol is −4.5°C [40].

Fig. 7 shows the wavelength shifts from the FBG sensor for all ethanol concentrations measured, as a function of the cooling bath temperature. Due to freezing-point depression in binary mixtures, the

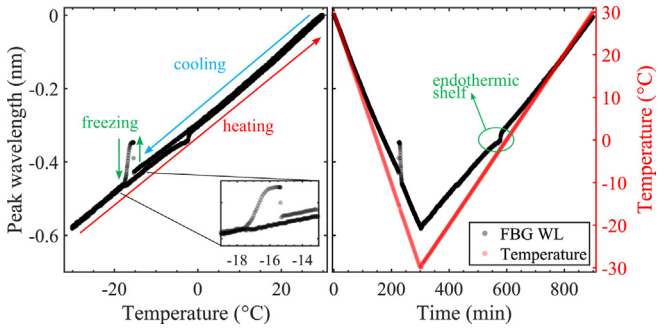

Fig. 6. The wavelength shifts of the FBG-sensor in 10% ethanol, as a function of temperature (left) and time (right). As in the case of pure water, the freezing event causes a short red-shift due to local heating. However, the sensor does not experience any significant strain from the solid formed. (For interpretation of the references to colour in this figure legend, the reader is referred to the web version of this article.)

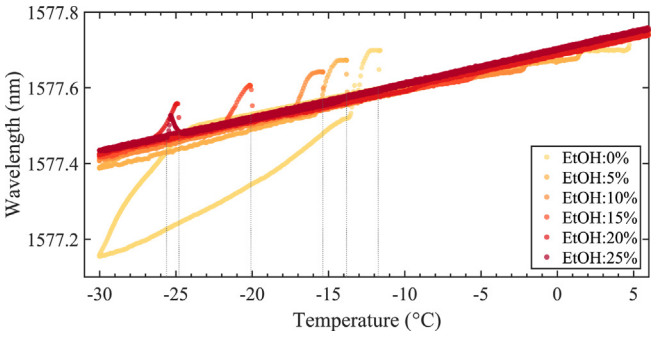

Fig. 7. The FBG peak wavelength shifts as a function of bath temperature for ethanol concentrations 0–25%. For higher concentrations, the freezing temperature is lowered. The 30% sample did not freeze and is therefore not shown, whereas the 25% sample froze first during the reheating phase.

higher concentrations freeze at lower temperatures. The freezing temperatures are indicated with grey lines. The 30% sample did not overcome the nucleation barrier in the temperature range measured and is therefore not shown, whereas the 25% sample first froze during the heating phase. The pure water shows clear evidence of compressive strain, but also the 5% sample seems to have some compression of the sensor.

The amount of super-cooling for each sample is summarized in Table 1. Based on the heat of fusion [34] and specific heat capacities for ethanol mixtures [41], the expected amount of ice initially formed was calculated using Eq. (6). For all ethanol concentrations, less than 23.5% of the water is able to freeze. That higher concentrations are able to produce more ice without additional heat transfer, is owed by the decrease in latent heat, increase in specific heat capacity, and increased super-cooling.

Although higher ethanol concentrations initially produce more ice, the freezing process was visually observed to be slower in the more concentrated samples. This is probably due to limited mass transfer at the solid–liquid interface, which also has been observed in forced convection studies [35,36]. These studies describe the creation of a “mushy zone” consisting of concentrated solute inclusions, which was also observed in the 30% ethanol sample used in this study.

The different melting points of water and low ethanol concentrations can again be observed by the endothermic shelves extending below the baseline, but at higher ethanol concentrations, the shelves become less pronounced. This is expected, as the melting temperature will increase as the ethanol concentration in the liquid phase decreases during melting.

By using the shift in the FBG wavelength prior to freezing as a function of temperature, a calibration curve can be established. With the calibration curve, and the data in Fig. 7, the actual temperature inside the sample can be estimated. This is shown in Fig. 8 as a function of time, for the freezing events (left) and melting (right). The calculation assumes that the shift is only a function of temperature, which clearly causes anomalies in the results for pure water. Because of the small strain seen after freezing for low ethanol concentrations, the temperature is underestimated on this interval. In the mixtures, the largest error is 4°C in the 5% sample.

The water measurement also shows a period of constant temperature during freezing, whereas the ethanol samples decrease in temperature during freezing (Fig. 8, left). The latter is expected as the ethanol concentration increases during the freezing process, which lowers the melting temperature. The temperature is therefore maintained at the decreasing melting temperature as long as the release of latent heat is faster than the heat transfer out of the sample to the temperature bath. This effect can be compared to the decrease in endothermic energy in Fig. 1 in the work of Takaizumi et al. [13] and was also observed in the freezing of biological specimens [6]. The effect is

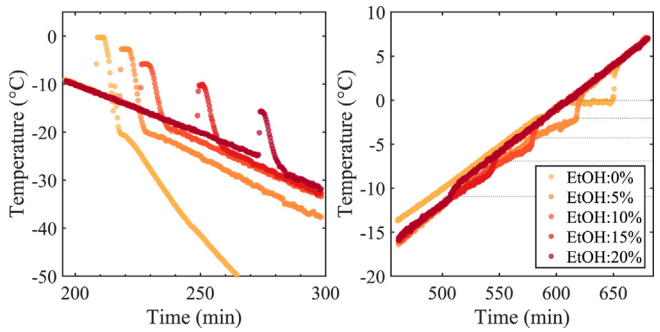

Fig. 8. The calculated local temperature within the sample for ethanol concentrations 0–20%, calculated by using the data prior to freezing as a baseline. Strain effects in the pure water sample causes a large disparity in the temperature estimation after freezing. The same but moderate effect can be seen in the 5% sample. The estimated melting temperatures can be compared to literature values indicated with grey lines.

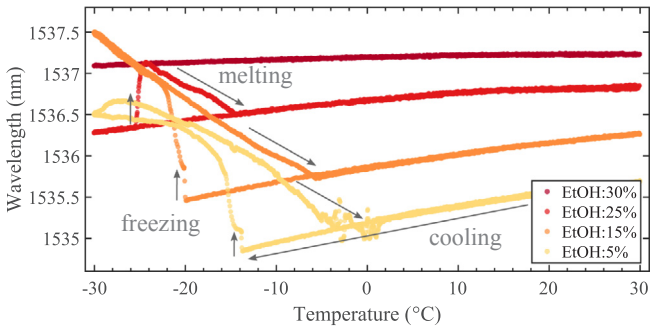

Fig. 9. The wavelength shifts of the TC dip as a function of *bath* temperature for selected ethanol concentrations. Because of the increased RI for higher concentrations, the liquid lines appear at higher wavelengths. The decreased sensitivity to temperature at higher concentrations is consistent with the decrease in thermo-optic coefficients [11]. Upon freezing, the dip continues to red-shift after the initial heating. The transition back to the liquid phase becomes more smooth for higher. concentrations.

evident already at 5%, but increases for higher concentrations. It should also be noted that due to the amount of ice initially formed, shown in Table 1, the plateaus of elevated temperature correspond to concentrations higher than before the nucleation. This causes the temperatures during the crystal growth phase to be lower than what is expected in the initial concentrations. Because the eutectic point is not reached in the measurement, the freezing will continue throughout the cooling stage. However, at one point, the amount of remaining liquid will be small enough and have a high enough concentration to slow down the phase transition sufficiently for the temperature to decrease down to that of the bath fluid. Samples with higher concentration will slow down earlier and therefore have a shorter period at the elevated temperature.

3.3. Melting of ethanol mixtures

Fig. 8 (right) shows the temperature inside the samples during the heating stage, where the endothermic shelves are seen to tilt increasingly for higher ethanol concentrations. The same reasoning as for the freezing process can be employed to explain this trend. That the temperature inside the sample is lower than that outside means that the endothermic thawing is more efficient at removing heat than what can be transferred from the bath fluid. This effect becomes more prominent for lower concentrations, as the change in ethanol concentration during melting is reduced. The tabulated melting points for the different concentrations are indicated with grey lines [40]. For pure water and the 5% sample, the estimated melting temperatures from the FBG sensor are approximately 0.3°C below the expected. The higher concentrations have a wider melting interval and the concentration in the liquid phase changes faster during melting. This makes it more difficult to determine the exact melting temperatures, but it also shows the importance of measuring the actual conditions when the temperature is scanned across the phase-transition interval.

3.4. Refractometric analysis in ethanol mixtures

The wavelength of dip 1 (TC sensor) in Fig. 3 is shown in Fig. 9 for selected ethanol concentrations. The measurement series is the same as what was presented in Fig. 7, but only the wavelength of the TC sensor is shown. The different mixtures exhibit different slopes due to the thermo-optic coefficient varying with the concentration. Contrary to the results for pure water (Fig. 5), the wavelength shows a strong red-shift upon freezing in the binary ethanol mixtures. The freezing event can be identified by the strong red-shift at the low-temperature end of each line. As was seen in Fig. 7, the 25% sample freezes during the heating stage, and the 30% sample does not freeze at all. When the samples are re-heated, the wavelength of the dip blue-shifts and ends up just below the liquid line.

The red-shift upon freezing can theoretically be described by either an increase in external RI or by strain. However, from Fig. 7 it is reasonable to conclude that only the pure water and the 5% ethanol sample are significantly affected by strain imparted by the solid phase. Because of the opposite sensitivity to strain, the small strain seen for low ethanol concentrations would red-shift the TC wavelength approximately an equal amount. Also, for higher ethanol concentrations, the transition back to the liquid phase becomes more smooth. Because of the geometry of the setup, where the heat transfer goes radially outwards through the test tube, the optical sensors are expected to be slightly warmer than the sample as they extend out of the temperature bath into room temperature. Since the solid phase is expected to be pure ice [12,14], it is therefore reasonable to assume that a concentrated ethanol mixture is left around the sensors. This assumption is supported by the fact that at −30°C there will still be concentrated liquid present, which will be true for temperatures above the eutectic. At the lowest temperature measured, it is therefore expected that the remaining liquid phase has an ethanol concentration of around 40% [40]. If pure ice were to surround the sensor, the blue-shift seen in Fig. 5 would be expected. This theory may also explain why the dip appears at slightly shorter wavelengths during the heating, compared to the cooling line. Due to the concentrated liquid phase that remains after the liquid-to-solid transition, ethanol evaporation may have occurred. This is supported by the 30% line which does not show the hysteresis. To estimate the melting temperatures from these results is difficult since the temperature is measured outside the sample, which was shown to differ from that inside.

This motivates a further analysis of the origin of the increased RI after freezing, which will be done in the following section.

3.5. Analysis of post-freeze results

By utilizing the curves prior to freezing, the wavelength shift as a function of ethanol concentration was found, at each temperature. With the assumption that the sensor always is in contact with a liquid phase, also after freezing, the ethanol concentration in the remaining liquid was calculated. The calculation followed these steps:

1. Each wavelength curve in Fig. 9 was fitted to a second-degree polynomial, using the data from 30°C down to each respective freezing point.
2. The fitted functions were extrapolated down to −30°C.
3. At each temperature step, a new function was found that describe the wavelength as a function of ethanol concentration.
4. A new vector was created from the 30% ethanol data that did not

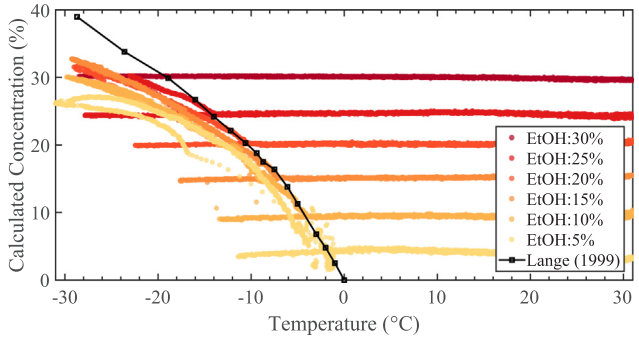

Fig. 10. The calculated ethanol concentrations surrounding the fiber-optic sensors before and after freezing, together with tabulated melting temperatures from [40]. In the liquid phase, the concentrations are constant, while after freezing the concentrations become functions of temperature. The horizontal axis shows the temperatures calculated from the FBG sensor output (Fig. 8).

freeze, which contain the estimated temperature inside the sample measured with the FBG sensor.

5. The temperatures from Step 4 were then used to find the actual ethanol concentration from the function defined in Step 3.
6. The resulting concentration was plotted as a function of the temperature measured inside the sample.

The resulting concentrations are shown in Fig. 10, together with the tabulated melting points of ethanol water mixtures from Lange's Handbook of Chemistry [40]. The estimated temperature from the FBG sensor inside the sample is plotted on the horizontal axis.

In the liquid phase the concentrations are constant, as is expected since this is the data that was used to calibrate the estimation. The amount of undercooling for each concentration is the difference between the lowest temperature of the horizontal (liquid) line and the tabulated melting points shown in black. For the concentrations 5–20%, the undercooling increases from 10 to 14°C, see Table 1. Following this trend, the 25% sample is expected to freeze at approximately −30°C, but in this case it did not overcome the nucleation barrier until later during the re-heating. This highlights the statistical nature of the phase transition.

The underestimation of the temperature from the FBG-sensor in the solid phase causes an underestimation of the ethanol concentrations on the same interval. However, the opposite strain effect on the TC-sensor will partly compensate for this effect. If the assumption of pure water in the solid phase is correct, the lines in Fig. 10 should therefore follow the tabulated melting points after freezing. That some of the lines (lower concentrations) lie below the tabulated data means that the average RI around the fiber is lower than what is expected. The reason for this is difficult to conclude, but it may indicate that the ice phase exists close enough to the fiber to displace some of the concentrated ethanol solution. This may also explain the increased deviation from the tabulated values at lower temperatures, where more of the remaining liquid around the fiber freezes. Air bubbles trapped close to the fiber would also decrease the effective concentration measured. The release of air bubbles may be the reason for the more erratic behavior of the 0% and 5% samples during melting, but does not explain the increased deviation at lower temperatures. Simulations done in previous work [25], show that the half-length of the evanescent field is 4–500 nm (optical intensity: ~350 nm), which defines the volume around the fiber that is probed. The sensor measures the average RI in this volume, and the effect is therefore a local phenomenon.

Upon heating, the estimated concentrations eventually approach and coincide within 0.1°C of the tabulated melting values. This may indicate that the ice closest to the sensors has melted and left only liquid in the volume probed by the evanescent field. The combined output from the dual-sensor setup can therefore be expected to be able to estimate melting points, limited by the accuracy of the two sensors and the temperature bath. The temperature measurement showed an RMSE of 0.15°C and the temperature bath is accurate within 0.25°C. Based on the RMSE of the wavelength determination, the sensor should be able to estimate the ethanol concentration within ± 0.1%, but strain and a non-linear RI sensitivity introduces additional errors for both sensors.

As the growth of the solid phase is random, it is also not certain that the two fiber-optic sensors are exposed to the same conditions. Placing both sensors on a single fiber would create a longer probe, but would reduce these uncertainties. The sensor response is also different from experiment to experiment, although the same general behavior can be observed.

Whereas this study has interpreted the sensor-system response based on known properties of the samples, the intended use of a sensor is generally the opposite i.e. to extract unknown information from the sensor response. In situations where the properties of the samples are known approximately, the sensors can aid in measuring or confirming the actual conditions. In most systems, assumptions or prior measurements will aid in understanding the output. Even though the interpretation of most measurements relies on some assumptions or prior measurements, the dual-fiber sensor system also offers some *a priori* information. Both the temperature and RI in the system can be explicitly determined in gasses and liquids, where strain effects can be neglected. In addition, the effective concentration around the sensors and the heat generation/absorption is implicitly given by the RI and temperature. In experimental situations there are also factors that are difficult to control, which affects the progression of phase transitions e.g. heat transfer. Even with the known melting temperatures for aqueous ethanol mixtures used in this study, the dynamic behavior of the samples is difficult to predict. The sensors ability to capture the unique progression of each measurement is therefore paramount in real-life systems.

4. Conclusions

A dual fiber-optic sensor system was presented, and demonstrated to be able to detect and characterize phase transitions in both pure liquids and binary mixtures. Mixtures of ethanol in the range of 0–30% were used to demonstrate the concept. The combination of a multi-mode interferometer with a fiber Bragg grating sensor was used to distinguish between RI, temperature and strain. The interplay between these parameters were used to extract the information that can be obtained about phase transitions, as well as the liquid and solid phases. By identifying the strain-free regions in the FBG sensor response, the changes in external RI can be estimated. This was especially important in the case of pure water, where compressive strain from thermal expansion was found to greatly thwart the temperature measurement. An indisputable explanation for the accelerated strain relaxation during the heating stage was not found, but conductive heat transfer through the fiber may be a contributing factor.

Visually, pure water seems to freeze instantaneously because of the rapid dendritic crystal growth. However, the sensors are able to resolve the transition fully, progressing from a monophasic liquid, through a biphasic liquid–solid state, to the solid state. It was noted that only the pure water exhibits a constant temperature during freezing, whereas the temperature gradually decreases for the ethanol mixtures. The effect is more pronounced for higher concentrations, and is expected due to freezing-point depression in binary mixtures. This is also apparent during melting, where the temperature remains constant until the transition is complete – an effect that becomes less pronounced at higher ethanol concentrations. Due to the dynamic nature of the experiment, the melting temperatures for different concentrations of ethanol were difficult to extract from each one of the two sensors. But through analysis of the combined response of the two sensors, the determined melting points agreed with the tabulated values within the

uncertainty of the experiment (0.25°C).

The system was also able to distinguish between pure liquids and binary mixtures, because of the partial freeze-out of the latter. This results in less, or no strain, and an increased concentration (increased RI) in the remaining liquid phase, whereas pure water showed a distinct reduction in RI due to the lower density of ice. The freezing process in pure water and low ethanol concentrations was found to be limited by heat transfer, whereas mass transfer was seen to be the limiting factor in mixtures with higher concentrations. The lack of strain after solidification also enabled an estimate of the concentration in the remaining liquid phase, which was found to lie below the literature values.

The amount of information extracted from the sensor system before, during and after a phase transition, emphasizes the benefits of having a dual-fiber setup.

Declaration of Competing Interest

None.

CRediT authorship contribution statement

Markus Solberg Wahl: Conceptualization, Methodology, Software, Validation, Formal analysis, Investigation, Writing - original draft, Visualization. **Øivind Wilhelmsen:** Conceptualization, Methodology, Validation, Formal analysis, Investigation, Resources, Writing - review & editing, Supervision, Project administration. **Dag Roar Hjelme:** Conceptualization, Methodology, Validation, Formal analysis, Investigation, Resources, Writing - review & editing, Supervision, Project administration.

References

[1] A. Sharma, V.V. Tyagi, C.R. Chen, D. Buddhi, Review on thermal energy storage with phase change materials and applications, Renew. Sustain. Energy Rev. 13 (2) (2009) 318–345, https://doi.org/10.1016/j.rser.2007.10.005.

[2] F.G. Qin, A.B. Russell, X.D. Chen, L. Robertson, Ice fouling on a subcooled metal surface examined by thermo-response and electrical conductivity, J. Food Eng. 59 (4) (2003) 421–429, https://doi.org/10.1016/S0260-8774(03)00002-5.

[3] S. Veesler, L. Lafferrère, E. Garcia, C. Hoff, Phase transitions in supersaturated drug solution, Organ. Process Res. Develop. 7 (6) (2003) 983–989, https://doi.org/10.1021/op034089f.

[4] Ø. Wilhelmsen, D. Berstad, A. Aasen, P. Nekså, G. Skaugen, Reducing the exergy destruction in the cryogenic heat exchangers of hydrogen liquefaction processes, Int. J. Hydrogen Energy 43 (10) (2018) 5033–5047, https://doi.org/10.1016/j.ijhydene.2018.01.094.

[5] K. Kvalsvik, D.O. Berstad, Ø. Wilhelmsen, Dynamic modelling of a liquid hydrogen loading cycle from onshore storage to a seaborne tanker, Science et Technique Du Froid Part F1477. (n.d.), doi: https://doi.org/10.18462/iir.cryo.2019.0019.

[6] D. Zaragotas, N.T. Liolios, E. Anastassopoulos, Supercooling, ice nucleation and crystal growth: a systematic study in plant samples, Cryobiology 72 (3) (2016) 239–243, https://doi.org/10.1016/j.cryobiol.2016.03.012.

[7] J. Dudak, J. Zemlicka, J. Karch, M. Patzelt, J. Mrzilkova, P. Zach, Z. Hermanova, J. Kvacek, F. Krejci, High-contrast X-ray micro-radiography and micro-ct of ex-vivo soft tissue murine organs utilizing ethanol fixation and large area photon-counting detector, Scient. Rep. 6 (2016) 30385, https://doi.org/10.1038/srep30385.

[8] G.C. Sosso, J. Chen, S.J. Cox, M. Fitzner, P. Pedevilla, A. Zen, A. Michaelides, Crystal nucleation in liquids: Open questions and future challenges in molecular dynamics simulations, Chem. Rev. 116 (12) (2016) 7078–7116, https://doi.org/10.1021/acs.chemrev.5b00744.

[9] F.K. Coradin, G.R. Possetti, R.C. Kamikawachi, M. Muller, J.L. Fabris, Etched fiber Bragg gratings sensors for water-ethanol mixtures: A comparative study, J. Microwaves Optoelectron. 9 (2) (2010) 131–143, https://doi.org/10.1590/S2179-10742010000200007.

[10] N. Nishi, S. Takahashi, M. Matsumoto, A. Tanaka, K. Muraya, T. Takamuku, T. Yamaguchi, Hydrogen-bonded cluster formation and hydrophobic solute association in aqueous solutions of ethanol, J. Phys. Chem. 99 (1) (1995) 462–468, https://doi.org/10.1021/j100001a068.

[11] S. Novais, M.S. Ferreira, J.L. Pinto, Determination of thermo-optic coefficient of ethanol-water mixtures with optical fiber tip sensor, Opt. Fiber Technol. 45 (July) (2018) 276–279, https://doi.org/10.1016/j.yofte.2018.08.002.

[12] K. Takaizumi, T. Wakabayashi, The freezing process in methanol-, ethanol-, and propanol-water systems as revealed by differential scanning calorimetry, J. Solution Chem. 26 (10) (1997) 927–939, https://doi.org/10.1007/BF02768051.

[13] K. Takaizumi, A curious phenomenon in the freezing-thawing process of aqueous ethanol solution, J. Solution Chem. 34 (5) (2005) 597–612, https://doi.org/10.1007/s10953-005-5595-6.

[14] S. Facq, F. Danède, B. Chazallon, Ice particle crystallization in the presence of ethanol: An in situ study by Raman and X-ray diffraction, J. Phys. Chem. A 117 (23) (2013) 4916–4927, https://doi.org/10.1021/jp4015614.

[15] K. Koga, H. Yoshizumi, Diffential scanning calorimetry (DSC) studies on the freezing processes of water-ethanol mixtures and distilled spirits, J. Food Sci. 44 (5) (1979) 1386–1389, https://doi.org/10.1111/j.1365-2621.1979.tb06444.x.

[16] H.J. Borchardt, F. Daniels, The application of differential thermal analysis to the study of reaction kinetics, J. Am. Chem. Soc. 79 (1) (1957) 41–46, https://doi.org/10.1021/ja01558a009.

[17] Anderson R., Adams R., Duggins B., Limitations of Thermocouples in Temperature Measurements, in: 25th ISA Anaheim CA (1979) 1–33.

[18] A. Dewaele, J. Eggert, P. Loubeyre, R. Le Toullec, Measurement of refractive index and equation of state in dense He, H2, H2O, and Ne under high pressure in a diamond-anvil cell, Phys. Rev. B 67 (9) (2003) 094112, https://doi.org/10.1103/PhysRevB.67.094112.

[19] D. Lee, R. Haynes, D. Skeen, Properties of optical fibres at cryogenic temperatures, Mon. Not. R. Astron. Soc. 326 (2) (2001) 774–780, https://doi.org/10.1046/j.1365-8711.2001.04630.x.

[20] W. Han, M. Rebow, D. Liu, G. Farrell, Q. Wu, Y. Ma, Y. Semenova, SNS optical fiber sensor for direct detection of phase transitions in C18H38 n-alkane material, Experimental Thermal and Fluid Science 109 (2018) 109854, https://doi.org/10.1016/j.expthermflusci.2019.109854 (November 2018).

[21] A. Millo, Y. Raichlin, A. Katzir, Mid-infrared fiber-optic attenuated total reflection spectroscopy of the solid—liquid phase transition of water, Appl. Spectrosc. 59 (4) (2005) 460–466, https://doi.org/10.1366/0003702053641469.

[22] R. Kumar, W. Han, D. Liu, W.P. Ng, R. Binns, K. Busawon, Y.Q. Fu, Z. Ghassemlooy, C. Underwood, K. Mahkamov, J. Yuan, C. Yu, H. Shu, X.A. Li, T. Guo, G. Farrell, Y. Semenova, Q. Wu, Optical fibre sensors for monitoring phase transitions in phase changing materials, Smart Mater. Struct. 27 (10) (2018) 105021, https://doi.org/10.1088/1361-665X/aaddba.

[23] P. Mani, A. Rallapalli, V.R. Machavaram, A. Sivaramakrishna, Monitoring phase changes in supercooled aqueous solutions using an optical fiber Fresnel reflection sensor, Opt. Exp. 24 (5) (2016) 5395, https://doi.org/10.1364/OE.24.005395.

[24] W. Han, M. Rebow, D. Liu, G. Farrell, Y. Semenova, Q. Wu, Optical fiber Fresnel reflection sensor for direct detection of the solid–liquid phase change in n-octadecane, Meas. Sci. Technol. 29 (12) (2018) 125107, https://doi.org/10.1088/1361-6501/aaeabb.

[25] M.S. Wahl, Ø. Wilhelmsen, D.R. Hjelme, Addressing challenges in fabricating reflection-based fiber optic interferometers, Sensors 19 (18) (2019) 4030, https://doi.org/10.3390/s19184030.

[26] A.D. Kersey, M.A. Davis, H.J. Patrick, M. LeBlanc, K.P. Koo, Fiber grating sensors, J. Lightwave Technol. 15 (8) (1997) 1442–1463, https://doi.org/10.1109/50.618377.

[27] S. Tripathi, A. Kumar, R. Varshney, Y. Kumar, E. Marin, J.-P. Meunier, Strain and temperature sensing characteristics of single-mode–multimode–single-mode structures, J. Lightwave Technol. 27 (13) (2009) 2348–2356, https://doi.org/10.1109/JLT.2008.2008820.

[28] L. Li, L. Xia, Z. Xie, L. Hao, B. Shuai, D. Liu, In-line fiber Mach-Zehnder interferometer for simultaneous measurement of refractive index and temperature based on thinned fiber, Sens. Actuat. A: Phys. 180 (2012) 19–24, https://doi.org/10.1016/j.sna.2012.04.014.

[29] Y. Saito, J.J. Wang, D.A. Smith, D.N. Batchelder, A simple chemical method for the preparation of silver surfaces for efficient SERS, Langmuir 18 (8) (2002) 2959–2961, https://doi.org/10.1021/la011554y.

[30] R.C. Kamikawachi, I. Abe, A.S. Paterno, H.J. Kalinowski, M. Muller, J.L. Pinto, J.L. Fabris, Determination of thermo-optic coefficient in liquids with fiber Bragg grating refractometer, Opt. Commun. 281 (4) (2008) 621–625, https://doi.org/10.1016/j.optcom.2007.10.023.

[31] E.S.d.L. Filho, M.D. Baiad, M. Gagné, R. Kashyap, Fiber Bragg gratings for low-temperature measurement, Opt. Exp. 22 (22) (2014) 27681, https://doi.org/10.1364/oe.22.027681.

[32] A.H. Harvey, J.S. Gallagher, J.M.H.L. Sengers, Revised Formulation for the Refractive Index of Water and Steam as a Function of Wavelength, Temperature and Density, J. Phys. Chem. Ref. Data 27 (4) (1998) 761–774, https://doi.org/10.1063/1.556029.

[33] N.E. Dorsey, Supercooling and Freezing of Water, US Department of Commerce, 1938.

[34] H. Kumano, T. Asaoka, A. Saito, S. Okawa, Study on latent heat of fusion of ice in aqueous solutions, Int. J. Refrig. 30 (2) (2007) 267–273, https://doi.org/10.1016/j.ijrefrig.2006.07.008.

[35] S. Fukusako, M. Yamada, A. Horibe, H. Kawai, Solidification of aqueous binary solution on a vertical cooled plate with main flow, Heat Mass Transf. 30 (3) (1995) 127–134, https://doi.org/10.1007/BF01476520.

[36] C. Tangthieng, F.B. Cheung, S.W. Shiah, Behavior of the two-phase mushy zone during freeze coating on a continuous moving plate, J. Heat Transf. 124 (1) (2002) 111–119, https://doi.org/10.1115/1.1420714.

[37] N.E. Dorsey, The freezing of supercooled water, Trans. Am. Philos. Soc. 38 (3) (1948) 247–328.

[38] T.R. Butkovich, Thermal expansion of ice, J. Appl. Phys. 30 (3) (1959) 350–353, https://doi.org/10.1063/1.1735166.

[39] J. Zhou, C. Liao, Y. Wang, G. Yin, X. Zhong, K. Yang, B. Sun, G. Wang, Z. Li, Simultaneous measurement of strain and temperature by employing fiber Mach-Zehnder interferometer, Opt. Exp. 22 (2) (2014) 1680, https://doi.org/10.1364/oe.22.001680.

[40] J.A. Lange, Lange's handbook of chemistry, 15th ed., McGraw-Hill Inc, New York, 1999.

[41] S. Rivkin, A. Winnikova, Die spezifischen Wärmen wässeriger Lösungen von Äthylalkohol, Chemie IngenieurTechnik 37 (1965) 557.